International Journal of Nanomedicine

Dovepress
Taylor & Francis Group

Open Access Full Text Article

ORIGINAL RESEARCH

Engineered Perfluorochemical Cancer-Derived Exosomes Loaded with Indocyanine Green and Camptothecin Provide Targeted Photochemotherapy for Effective Cancer Treatment

Yu-Hsiang Lee[1–3], Cheng-You Huang[1]

[1]Department of Biomedical Sciences and Engineering, National Central University, Taoyuan City, Taiwan, Republic of China; [2]Department of Chemical and Materials Engineering, National Central University, Taoyuan City, Taiwan, Republic of China; [3]Department of Medical Research, Cathay General Hospital, Taipei City, Taiwan, Republic of China

Correspondence: Yu-Hsiang Lee, Department of Biomedical Sciences and Engineering, National Central University, No. 300, Jhongda Road, Taoyuan City, 320317, Taiwan, Republic of China, Tel +886-3-422-7151 Ext# 27755, Fax +886-3-280-4627, Email yuhsianl@ncu.edu.tw

Background: Cancer treatments are still limited by various challenges, such as off-target drug delivery, posttreatment inflammation, and the hypoxic conditions in the tumor microenvironment; thus, the development of effective therapeutics remains highly desirable. Exosomes are extracellular vesicles with a size of 30–200 nm that have been widely applied as drug carriers over the last decade. In this study, melanoma-derived exosomes were used to develop a perfluorocarbon (PFC) drug nanocarriers loaded with indocyanine green (ICG) and camptothecin (CPT) (ICFESs) for targeted cancer photochemotherapy.

Methods: The ICFESs were fabricated by emulsification approach and characterized through instrumental detection. The capabilities of the ICFESs on tumor targeting, intratumoral retention, and cancer photochemotherapy were evaluated using melanoma tumor-bearing mice in association with histological studies and serum marker analyses.

Results: ICFESs can be rapidly internalized by homologous melanoma cells, induce hyperthermia and increase the yield of singlet oxygen upon exposure to near-infrared (NIR) irradiation. After 5 min of NIR exposure and 24 h of in vitro culture, ICFESs encapsulating ≥ 10/10 μM [ICG]/[CPT] effectively killed more than 70% of the cancer cells, inducing greater mortality than that caused by a 4-fold higher dose of CPT alone. In a murine melanoma model, we demonstrated that ICFESs indeed targeted homologous tumors with prolonged intratumoral retention compared with free ICG in vivo. Moreover, tumor growth was significantly arrested by ICFESs containing 40/40 μM [ICG]/[CPT] in combination with 30 sec of NIR exposure without systemic toxicity, and the resulting tumors were approximately 15-fold smaller than those treated for 14 days with 40 μM free CPT alone.

Conclusion: We suggest that the aforementioned anticancer efficacy was achieved via a dual-stage mechanism, phototherapy followed by chemotherapy. Taken together, the developed ICFESs are anticipated to be highly applicable for clinical cancer treatment.

Keywords: exosome, photochemotherapy, perfluorocarbon, hypoxia, homologous targeting, NIR irradiation

Introduction

Combined photo- and chemotherapy via the coadministration of photosensitizers and anticancer drugs, known as photochemotherapy, has long been recognized as a feasible strategy to treat various types of cancers, such as lung, skin, and breast malignancies.[1–3] Photochemotherapy is particularly suitable for clinical applications because chemotherapy is currently the mainstay treatment for the majority of solid and hematological carcinomas, whereas phototherapies, including photodynamic therapy (PDT) and photothermal therapy (PTT), are a safe and effective anticancer adjuvants with the advantages of noninvasiveness, high spatiotemporal control, and minor side effects compared with other

Received: 13 November 2024
Accepted: 3 January 2025
Published: 8 January 2025

Graphical Abstract

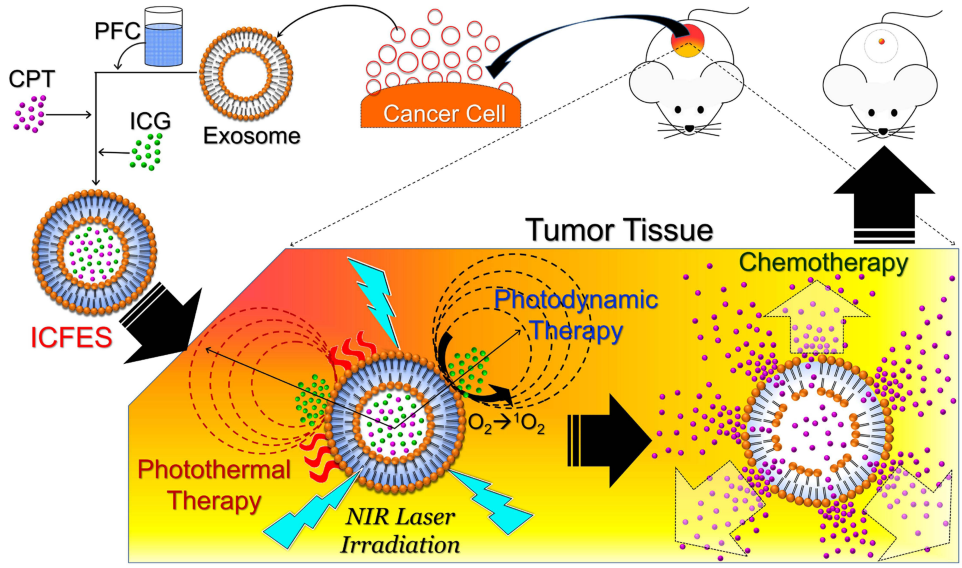

treatment modalities.[4] In general, PTT induces hyperthermia (> 42 °C) to ablate cancer cells,[5,6] whereas PDT hinders cellular metabolism, DNA replication, and tumor angiogenesis through the generation of reactive oxygen species (ROS).[7,8] During photochemotherapy, anticancer drugs can provide sustained, synergistic tumoricidal effects to eliminate the surviving cancer cells after laser irradiation. Moreover, phototherapy can reduce the effective dose of the chemotherapeutics and extenuate its systemic chemotoxicity.[9] Furthermore, phototherapy may induce an adaptive immune response by releasing damage-associated molecular patterns (DAMPs),[10] which is highly favorable for subsequent anticancer effects. However, challenges such as the hypoxic nature of the tumor microenvironment (TME) and the lack of an efficient and safe carrier for the delivery of multiple agents remain considerable barriers for both treatment modalities.

Hypoxia is a hallmark of cancer and present in a variety of tumors, including pancreatic cancer, lung cancer, breast cancer, and melanoma tumors.[11–14] Intratumoral hypoxia is usually caused by hyperproliferating cancer cells and deformation of the neoplastic vasculature, which dramatically decreases oxygen diffusion in the TME.[15] Such hypoxic conditions may induce the hypoxia-inducible factor (HIF) pathway to reprogram cancer cell metabolism[16] and consequently trigger chemoresistance, tumor recurrence, and metastasis.[17–19] On the other hand, hypoxia is highly unfavorable for ROS generation, which greatly restricts PDT; in contrast, PDT may further aggravate the hypoxic conditions in tumors and result in a poor treatment outcomes.[20] These circumstances indicate that oxygen plays a crucial role in photochemotherapy, and an effective method for oxygen delivery to the TME is still highly demanded nowadays.

Nanoencapsulation may be a feasible strategy by which multiple agents can be stabilized and delivered to tumors simultaneously since nanometer-sized carriers can enhance the stability, safety, and bioavailability of the encapsulated payload.[21] Among the various types of nanovehicles, exosomes, which are membrane-derived vesicles with diameters of 30–200 nm, are feasible drug delivery vectors that have gained increasing attention in recent decades because of their excellent bioavailability and homologous targeting properties.[22] Exosomes carrying multiple signaling molecules, including RNAs, proteins, and lipids, form in multivesicular bodies inside cells and naturally function as intercellular messengers.[23,24] Cell-derived exosomes have exceptional abilities, as they can rapidly interact with cellular membranes,[25] avoid phagocytic clearance,[26] and induce tropism to transport payloads to their target tissue, such as tumors.[27,28] Therefore, exosomes can serve as drug carriers with an "invisibility cloak" for the loaded therapeutic agents for targeted anticancer drug delivery. Indeed, exosomes have been extensively exploited as delivery vehicles for a variety of anticancer agents, including nucleic acids,[29,30] proteins,[31,32] and other compounds.[33,34]

To overcome the aforementioned challenges in cancer treatment, in this study, we sought to design and fabricate indocyanine green (ICG) and camptothecin (CPT) coloaded perfluorocarbon (PFC) cancer-derived exosomes, named ICFESs, and explore their applicability for cancer photochemotherapy. Near-infrared (NIR) was applied as the light source since it can penetrate deeper into tissue than can visible light or ultraviolet (UV) light.[35] CPT is a USFDA-approved anticancer drug commonly used for melanoma treatment.[36,37] ICG is a USFDA-approved NIR fluorophore that emits fluorescence in the range of 650–850 nm and has been extensively utilized for both cancer diagnosis[38–40] and anticancer phototherapy.[41–43] However, the drawbacks of ICG, including its thermal- and photo-susceptibility, rapid clearance in vivo, and dose-dependent aggregation properties, seriously limit its utility in the clinic.[44,45] PFC is a fluorine-substituted hydrocarbon derivative that was employed as the oxygen storage medium in ICFES because its oxygen dissolubility (35–44 mmol L^{-1}) is ~20-fold greater than that of water (2.2 mmol L^{-1}).[46] Therefore, we anticipate that the developed ICFES is a promising multifunctional anticancer agent that can 1) protect the encapsulated ICG from disintegration, 2) simultaneously transport CPT and ICG to tumors in a targeted manner, 3) promote both PDT and chemotherapy due to the reduction in hypoxia mediated by PFC, and 4) provide an anticancer effect with reduced chemotoxicity since combination phototherapy decreases the effective dose of the chemical drug. The hypotheses described above are comprehensively investigated in this paper.

Materials and Methods

Cell Culture

The murine melanoma B16F10 cells and hepatic FL83B cells were purchased from the Bioresource Collection and Research Center (Hsinchu, Taiwan ROC). B16F10 cells were cultivated in Dulbecco's modified eagle medium (DMEM) supplemented with sodium bicarbonate (1.5 g L^{-1}), extracellular vehicles (EV)-free fetal bovine serum (FBS; 10%), and penicillin/streptomycin (100 U mL^{-1}). FL83B cells were cultured in Ham's F12K medium supplemented with FBS (10%), L-glutamine (2 mm), sodium bicarbonate (1.5 g L^{-1}), and penicillin/streptomycin (100 U mL^{-1}). Both cell lines were maintained at 37 °C with 5% CO_2 and 100% humidity.

Exosome Collection

B16F10 cellular exosomes (BCEs) were harvested via ultrafiltration as reported previously.[47] Briefly, the B16F10 cell culture supernatant was centrifuged at 1500 × *g* and 4 °C for 10 min, after which the supernatant was collected and subjected to centrifugation again at 10000 × *g* and 4 °C for 10 min. The resulting supernatant was collected and concentrated using ultrafiltration columns (100K MWCO Macrosep® Advance, Pall Corp., Port Washington, NY, USA) according to the manufacturer's instructions. The BCEs were extracted from the concentrated medium using qEV2-70 nm columns (Izon Science, Addington, New Zealand) and concentrated using the Microsep™ Advance Kit (Pall Corp.). Finally, the BCEs were suspended in 1 mL of phosphate-buffered saline (PBS) and immediately subjected to a BCA assay for protein quantification.

Preparation and Characterization of the ICFESs

The ICFESs were fabricated via a one-pot synthetic approach. In brief, 1 mL of PBS was added by 100 μL of a 50% (v/v) solution of ICG (0.2 wt%, Sigma–Aldrich, St. Louis, MO, USA) in methanol, 100 μg of CPT (Sigma–Aldrich), perfluorooctyl bromide (PFOB; Sigma–Aldrich), and BCEs (at a PFOB:BCE protein ratio of 400:1 (w/w)) in the dark at room temperature. Afterward, the mixture was homogenized for 6 min and then maintained at 37 °C for one hour to yield the ICFESs. After washing twice with deionized (DI) water followed by centrifugation at 6000 × *g* and 4 °C for 10 min, the ICFESs were resuspended in 1 mL of DI water and stored in the dark at 4 °C until use.

The morphologies of the BCEs and ICFESs were observed via scanning electron microscopy (SEM) and transmission electron microscopy (TEM) with uranyl acetate (UA; 2%) staining. The sizes and zeta potentials of the BCEs and ICFESs were measured by dynamic light scattering (DLS). The encapsulation and loading efficiencies of ICG and CPT in the ICFESs were assessed spectrophotometrically as described elsewhere.[9]

ICFES stability was assessed by measuring the changes in both the quantity (N_P) and size of the material after storage at 4 °C and 37 °C for 7 days. ICFES size was measured by DLS every 48 h, whereas N_P was estimated according to the following formula:

$$N_P = \frac{X_P \times V}{V'} \tag{1}$$

where X_P represents the volume ratio of PFOB in the ICFES sample and can be determined via a gravimetric method in combination with regression analysis as described previously.[48] V and V' represent the volume of the entire ICFES sample and a single spherical ICFES entity, respectively. The exosomal characteristics of the ICFESs were detected by examining the expression of the exosomal markers tumor susceptibility gene 101 (TSG101) and cluster of differentiation 9 (CD9) via Western blotting.

Evaluation of the Cell Uptake Efficiency of the ICFESs

Twenty-four hours after being seeded in 6-well culture plates, B16F10 and FL83B cells (each 5×10^5 cells per well) were separately treated with an equal amount of ICFES ([ICG]/[CPT] = 5/5 μM) and incubated at 37 °C for 4 h. Afterward, the cells in both groups were washed twice with PBS and subjected to spectrofluorometric analysis (excitation/emission wavelengths = 730/818 nm) for detection of the intracellular fluorescence intensity of ICG which is represented by RFUs. The cellular uptake efficiency of ICFES was quantitatively analyzed after normalization to the blank sample.

Assessments of ICG Degradation and Kinetics of CPT Release from the ICFESs

ICFES samples with known absorbance values at λ = 780 nm were placed at separately 4 °C and 37 °C in the dark. After 3, 6, 12, 24, and 48 h, the ICFES samples under each temperature condition were centrifuged at 6000 × *g* and 4 °C for 30 min, after which the precipitates and the supernatants were collected separately. The precipitates were resuspended in DI water and subjected to spectrophotometric analysis at λ = 780 nm to determine the amount of ICG remaining in the ICFESs, whereas the supernatant was spectrophotometrically analyzed at λ = 370 nm to determine the amount of CPT released. In addition, the degradation rate coefficient (K_d) for both ICG encapsulated in the ICFESs and free ICG maintained at 4 °C or 37 °C was calculated according to the following equation:[45]

$$\frac{C(t)}{C(0)} = \exp(-K_d \times \mathrm{t}) \tag{2}$$

where $C(0)$ and $C(t)$ denote the concentrations of ICG in the medium (ICFES or DI water) at time $t = 0$ and at a specific time $t > 0$, respectively.

To assess how NIR irradiation affects drug release, the designated dose of ICFES was exposed to NIR, and the amount of CPT in the supernatant was measured via spectrophotometry (λ = 370 nm) every 60 sec for 5 min. NIR treatment was performed using an 808 nm laser with an output intensity of 6 W cm^{-2}. The temperature of the ICFES system was continuously measured using a thermocouple throughout the 5 min of NIR exposure.

Assessments of Hyperthermia and Singlet Oxygen Yields of the ICFESs Upon NIR Irradiation

ICFESs containing 0 (DI water only), 2.5, 5, 10, 20, 40, and 80 μM ICG in 200 μL of DI water were separately placed in 96-well culture plates at ambient temperature in the dark and exposed to NIR light irradiation with an 808 nm laser at an intensity of 6 W cm^{-2}. Moreover, the temperature of each system was measured using a thermocouple every 30 sec for 5 min. Furthermore, the production of singlet oxygen in each system was detected using a singlet oxygen sensor green (SOSG) kit (Life Technologies, Carlsbad, CA, USA) every 60 sec for 5 min.

Assessment of the Photochemotoxicity of the ICFESs

Twenty-four hours after being seeded in 96-well culture plates, B16F10 cells (5×10^4 cells per well) were treated with NIR, free ICG + NIR, CPT, or ICFES ± NIR, in which the NIR exposure was conducted using an 808 nm laser at an

intensity of 6 W cm^{-2} for 5 min. The concentrations of the free agents (ICG and CPT) used in the assay were equal to the ICG/CPT doses in ICFES ([ICG]/[CPT] = 0/0 (blank), 2.5/2.5, 5/5, 10/10, 20/20, and 40/40 μM). The ICG/CPT doses in ICFES were calculated on the basis of their encapsulation efficiencies, as described above. The viability of the cells in each system was assessed by both MTT and calcein-AM/propidium iodide staining assays 24 h after treatment.

Animal Model

C57BL/6 mice (32 ± 5 g, 6–7 weeks) were purchased from BioLASCO (Taipei, Taiwan ROC) for the animal assay. Cancer grafting was conducted by subcutaneously injecting 5×10^6 B16F10 cells into the flank region of each mouse, and the tumor size (V) was calculated every 48 h according to the formula $V = (W^2 \times L)/2$, where W and L denote the minor and major axes of the tumor, respectively. The experimental mice were subjected to in vivo assays when their tumor sizes ranged from 80–100 mm^3. All of the animal protocols complied with the guidelines reviewed by the Institutional Animal Care and Use Committee at Cathay General Hospital (Taiwan ROC, approval number: CGH-IACUC-113–003).

Analyses of Homotypic Targeting and Intratumoral Retention Efficacies of the ICFESs in vivo

ICG solution or ICFESs (50 μL, each containing 80 μM ICG) was injected intratumorally or intravenously via the tail into the B16F10 tumor-bearing mice. The fluorescence intensity of ICG in the groups that received an intravenous injection was analyzed after 1, 4, 16, and 24 h using an IVIS imaging system (In-Vivo Xtreme II™, Bruker, Billerica, MA, USA), whereas that in the groups that received an intratumoral injection were monitored every 48 h for 7 days. Furthermore, the livers, lungs, kidneys, hearts, spleens, and tumors of the intratumorally injected mice were harvested after sacrifice on the 7th day and subjected to fluorescence detection using the IVIS imaging system.

Evaluation of the in vivo Tumoricidal Efficacy of the ICFESs

B16F10 tumor-bearing mice were intratumorally injected with 50 μL of PBS, free ICG + NIR, CPT, ICFES, or ICFES + NIR (n = 4 in each group), and NIR irradiation (808 nm; 6 W cm^{-2}) was applied to the appropriate groups for 30 sec. The doses of free ICG and CPT were equal to the [ICG]/[CPT] doses in ICFES, which were determined on the basis of the in vitro photochemotoxicity test results. Each agent was administered intratumorally every 48 h for two weeks. The tumor size, physical appearance, and body weight of each experimental mouse were evaluated every 48 h prior to treatment, and the tumors and organs, including the liver, lung, kidney, heart, and spleen, were excised after the mice were sacrificed for histological and biocompatibility studies.

Histological Analyses

Tissue specimens were prepared according to standard histological procedures, as described previously.[49] All of the tissue samples were stained with hematoxylin and eosin (H&E), and the tumors were further examined via caspase-3 and Ki-67 immunohistochemical (IHC) assays. All of the staining images were processed with Motic DSA software (Motic, Kowloon, Hong Kong), and the expression levels of Ki-67 and caspase-3 in each tumor tissue sample were quantitatively analyzed using ImageJ.

Evaluation of the Systemic Toxicity of the ICFESs

To assess the systemic toxicity of ICFES, the aspartate aminotransferase (AST), alanine aminotransferase (ALT), blood urea nitrogen (BUN), and creatinine (CRE) levels, as well as the platelet (PLT), white blood cell (WBC), and red blood cell (RBC) numbers, in all the experimental mice were measured using a serum bioanalyzer (FUJI DRI-CHEM 4000i, FUJIFILM, Tokyo, Japan) three days before the experiment (day −3) and after 14 days of treatment (day 14). In addition, for the mice treated with chemo drugs, the amount of CPT in each of their organs (liver, lung, kidney, heart, and spleen) was measured via spectrophotometry analysis after sacrifice.

Statistical Analysis

MedCalc software (version 17.2) was used for data analysis, and the results are presented as the means ± standard deviations (SDs) with n ≥ 3. Comparisons between two groups were made via Student's *t* test followed by Dunnett's post hoc test. $P < 0.05$ was considered statistically significant throughout the study.

Results and Discussion

Fabrication and Characterization of the ICFESs

The fabrication of the ICFESs is schematically presented in Figure 1 (I). Based on the hydrophilic/hydrophobic characteristics of the agents, we anticipate that the PFOB was entrapped in the interlayer of the ICFES, while both ICG and CPT were encapsulated in the central/inner water phase of the ICFES, as illustrated in Figure 1 (I). Figure 1 (II) shows SEM and TEM images of the BCEs and ICFESs, which reveal that the engineered ICFESs (Figure 1 (II), b and d) retained the granular morphology of the BCEs after the drug encapsulation process including sonication and high-speed centrifugation, but show a rougher surface (Figure 1 (II), a and b) and plumper shape (Figure 1 (II), c and d) compared to the BCEs. The ICFES sample appeared as a green emulsion as illustrated in Figure 1 (III/a). The dark precipitate and clear supernatant after centrifugation shown in Figure 1 (III/b) indicated that ICG and CPT were certainly encapsulated in

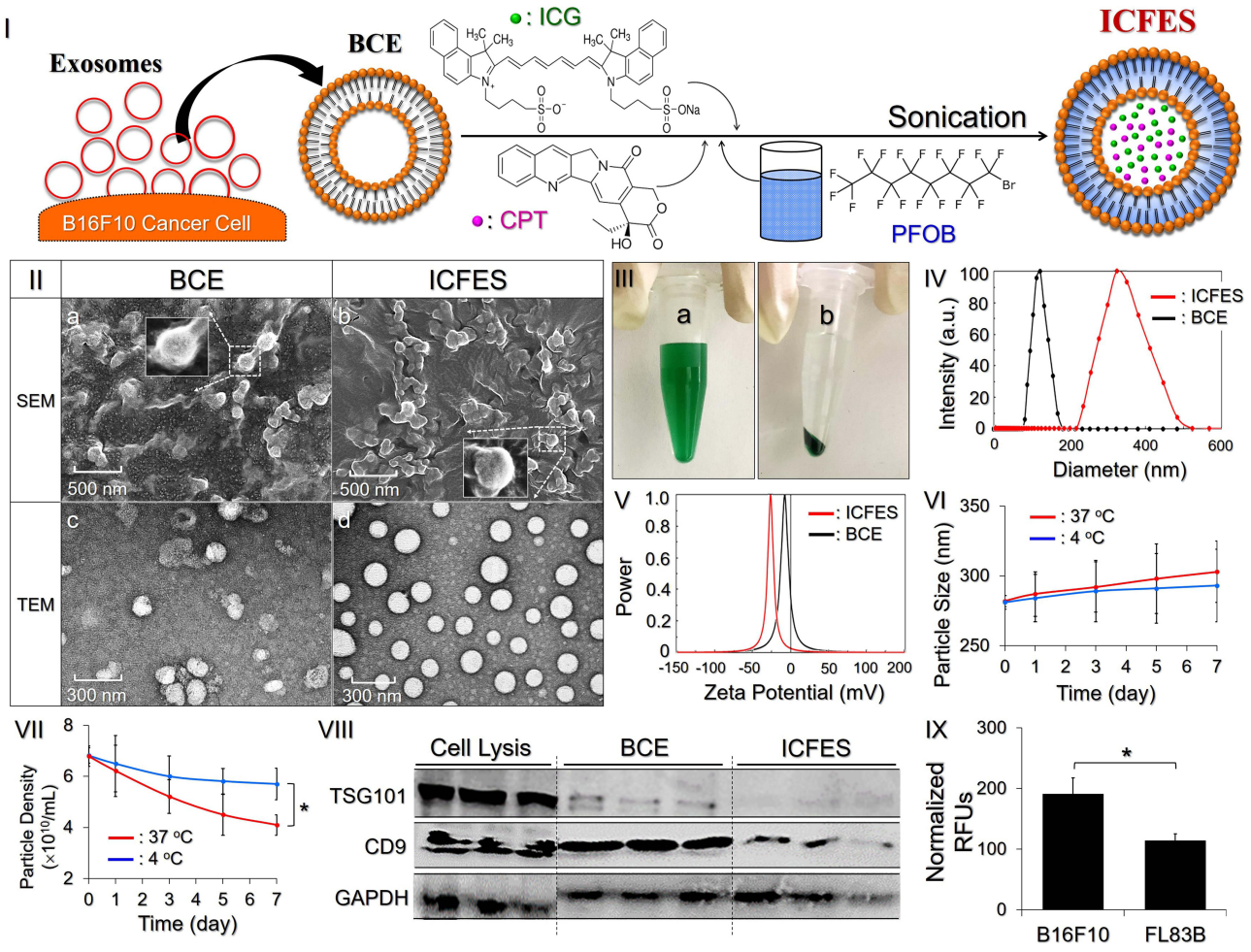

Figure 1 Fabrication and characterization of the ICFESs. (**I**) Schematic of ICFES fabrication. (**II**) SEM (a and b) and UA-stained TEM (c and d) images of the BCEs (a and c) and ICFESs (b and d) at 40,000× and 100,000× magnification, respectively. (**III**) Visual appearance of the ICFES sample before (**a**) and after (**b**) centrifugation. (**IV** and **V**) Size distributions (**IV**) and zeta potentials (**V**) of the BCEs and ICFESs determined by DLS. (**VI** and **VII**) Variations in the size (**VI**) and exosome density (**VII**) of the ICFESs after incubation at 4 °C or 37 °C for 7 days. The values presented are the means ± SDs (n = 3) **P* < 0.05. (**VIII**) Images of Western blotting for the proteins of TSG101, CD9, and GAPDH expressed in the B16F10 cell lysate, BCEs, and ICFESs. (**IX**) Verification of ICFES homology. The fluorescence intensity of ICG in the ICFES-treated FL83B and B16F10 cells was detected by spectrofluorometry and is quantitatively represented by RFUs. The values presented are the means ± SDs (n = 3) **P* < 0.05.

the exosomes. DLS analysis revealed that the BCEs and ICFESs had sizes of 136.4 ± 35 nm and 281.3 ± 86 nm (Figure 1 (IV)) and zeta potentials of −5.6 mV ± 8.1 mV and −30.5 mV ± 10 mV (Figure 1 (V)), respectively. We attributed the increase in size of the ICFESs to chemical encapsulation, whereas the greater negative charge of the ICFESs was likely due to the adsorption of anionic ICG on its surface. The encapsulation efficiencies of ICG and CPT in the ICFESs were 98.8 ± 1.22% and 85.6 ± 3.47%, respectively, while their loading rates were 0.27 ± 0.05 wt% and 0.13 ± 0.02 wt%, respectively.

The stability of the ICFESs was assessed by detecting the changes in size and particle number after storage at different temperatures over time. After incubation at 4 °C and 37 °C for 7 days, the ICFESs slightly increased in size by 4.27% and 7.45%, respectively (Figure 1 (VI)), whereas the density dramatically decreased by 16.4% and 39.6%, respectively (Figure 1 (VII)). The quantity of ICFES significantly changed at 4 °C and 37 °C ($P < 0.05$), indicating that the ICFESs are sensitive to the environmental temperature.

The exosomal integrity of the ICFESs after sonication was evaluated via Western blotting. As presented in Figure 1 (VIII), the typical exosome markers TSG101 and CD9[50,51] were expressed in the BCE and ICFES samples, but the expression level of TSG101 in the ICFES samples was much lower than that of CD9. This observation was attributed to the fact that TSG101 is an intraexosomal/cytosolic biomarker rather than a transmembrane protein such as CD9. It has been known that sonication-mediated drug encapsulation reorganizes the exosomal loads, which leads to exchange of the substances inside and outside the exosomes[52] and the subsequent loss of cytosolic molecules; therefore, trace amounts of TSG101 were detected in the ICFES samples.

Homologous Targeting Effect of the ICFESs

The uptake of the ICFESs by the BCE source cells (B16F10 cells) was assessed by measuring the fluorescence intensity of ICG and comparison with the results obtained with murine hepatocytes. As shown in Figure 1 (IX), the RFUs of the B16F10 cells was 1.7-fold ($P < 0.05$) higher than that of the FL83B cells after 4 h of ICFES treatment, indicating that the ICFESs are more rapidly internalized by the cells from which the exosomes were derived than by other types of cells in vitro. These results demonstrate the homologous targeting property of the ICFESs to their parental cells, and we attributed this efficacy to the function of CD9 as reported previously.[53]

Thermal Stability of the ICG Encapsulated in the ICFESs

Figure 2 (I/a) shows the variations in the UV–Vis spectra of free ICG and ICG entrapped in the ICFESs after incubation at 4 °C or 37 °C for 48 h. According to the quantitative analysis, ICG degradation increased with increasing temperature and was remarkably greater in aqueous solution than when encapsulated in ICFES at the same temperature (Figure 2 (I/b)). These results show the photo- and thermosensitivity of ICG.[44,45]

In contrast to the high degradability of ICG, > 60% of the encapsulated ICG was retained in the ICFESs after maintenance at 37 °C for 48 h, and this retention ratio was even greater than that obtained from the free ICG under 4 °C storage for 48 h. Analysis of the degradation rate coefficient (Table 1) showed that the thermal stability of the ICG encapsulated in the ICFESs was approximately 3.4- ($P < 0.05$) and 2.9-fold ($P < 0.05$) greater than that of free ICG after 48 h of incubation at 4 °C and 37 °C, respectively, demonstrating that the thermal stability of ICG increases dramatically upon exosomal encapsulation.

Release Kinetics of the CPT Encapsulated in the ICFESs Upon NIR Irradiation

Figure 2 (II/a) shows the spectra of CPT after it was released from the ICFESs into the supernatant during 48 h of incubation under different temperature conditions. A biphasic release pattern, with rapid release occurring during the first three hours followed by slow sustained release, was observed at both temperatures, resulting in cumulative release rates of 15% and 47% at 4 °C and 37 °C, respectively (Figure 2 (II/b)). These data indicate that higher temperature promotes drug release from the ICFESs because heat increases nanoparticle mobility and the incidence of collisions, leading to breakdown of the exosome and drug leakage.

The CPT release kinetics upon NIR exposure were further analyzed to assess the photochemical efficiency of the ICFESs. As presented in Figure 2 (III), drug release occurred quickly with a biphasic pattern upon NIR irradiation, and the cumulative

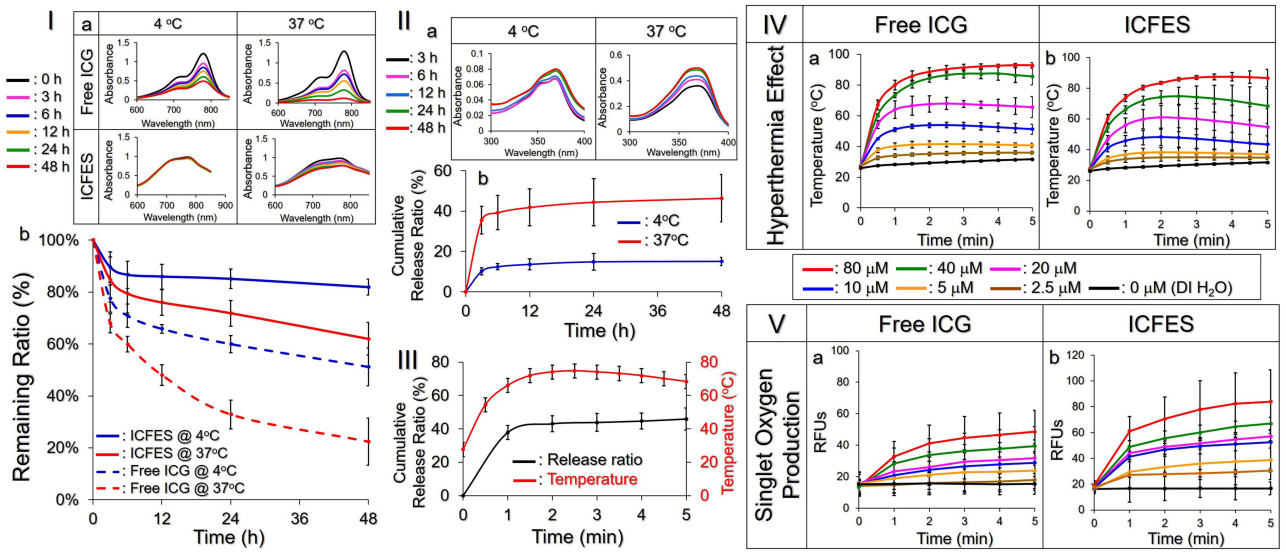

Figure 2 Thermal stability and phototherapeutic effects of the ICFESs in vitro. (I) a: UV–Vis spectra of free ICG and the ICFESs showing ICG degradation over 48 h at different temperatures. The absorbance at λ = 780 nm in each spectrum indicates the amount of ICG in the sample. b: Ratio of the amount of ICG remaining in aqueous solution and the ICFESs after incubation at 4 °C and 37 °C for 48 h. (II) a: UV–Vis spectra of the ICFES supernatant showing the release of CPT over 48 h at different temperatures. The absorbance at λ = 370 nm in each spectrum indicates the amount of CPT in the supernatant. b: Kinetics of the release of CPT encapsulated in ICFES after incubation at 4 °C or 37 °C for 48 h. (III) Kinetics of the release of CPT encapsulated in ICFES upon NIR irradiation for 5 min (black curve). The red curve indicates the change in temperature of the exosomal system over the 5 min of NIR exposure. (IV and V) Hyperthermia (IV) and singlet oxygen yield (V) produced from different concentrations of free ICG or ICFESs over 5-min NIR irradiation. The values in (I)–(V) are the means ± SDs (n = 3).

release of CPT was approximately 46% after 5 min of NIR exposure. Considering that temperatures > 70 °C (Figure 2 (III)) are detrimental to the exosomal membrane,[54] we assume that upon NIR treatment, the ICFESs quickly disintegrated and thus released large amounts of CPT during NIR irradiation. These data indicate that CPT release efficiency from the ICFESs can be greatly promoted by NIR irradiation.

Hyperthermia and Yield of Singlet Oxygen Induced by the ICFESs Upon NIR Irradiation

Figure 2 (IV) shows the thermoresponsive profiles of free ICG and ICFESs with different ICG concentrations upon NIR irradiation. The systemic temperature increased to ≥ 42 °C within 5 min of NIR irradiation in both groups when the ICG concentration was ≥ 10 μM. However, the thermal effectiveness of the ICFESs was lower than that of free ICG at an equal concentration. We speculate that this occurred because only some of the ICG in the nanocarrier was irradiated due to shielding by the exosomes, which is in contrast to what occurred in the aqueous solution where all of the ICG molecules react simultaneously upon NIR exposure, leading to reduced hyperthermia efficacy. Furthermore, since PFOB has a higher evaporation enthalpy (~45.6 KJ mol^{-1}) than water (40.7 kJ mol^{-1}), the temperature change in PFOB nanocarrier (ICFES) is lower than that in aqueous solutions (free ICG). Moreover, lipocarrier decomposition is an endothermic process that may decrease the systemic enthalpy;[55] therefore, the change in the ICFES temperature is

Table 1 Degradation Percentages and K Values of Free ICG and ICG Encapsulated in the ICFESs After Incubation at 4 °C and 37 °C for 48 h

Group	Temperature (°C)	Degradation (%)	K_d (h^{-1})
Free ICG	4	49.8%	0.0141
	37	77.6%	0.0312
ICFES-encapsulated ICG	4	18.1%	0.0042*
	37	38.3%	0.0107*

Note: *P < 0.05 compared with the free ICG group at the same temperature.

https://doi.org/10.2147/IJN.S505458

anticipated to be moderate compared with that in aqueous solutions. Nonetheless, these results indicate that ICFES can induce hyperthermia in a dose-dependent manner upon NIR exposure and consequently provide PTT.

Figure 2 (V) shows the singlet oxygen production efficacies of free ICG and the ICFESs during 5 min of NIR exposure. ICFES rapidly generated singlet oxygen within one minute of NIR irradiation with yields approximately 70% higher than those produced with an equal concentration of free ICG on the basis of RFU analysis. We reason that this increased ROS generation was mainly due to the PFC component, since PFOB has about 24-fold higher oxygen dissolubility (53 mmol O_2 L_{PFOB}^{-1}) than water (2.2 mmol O_2 L_{Water}^{-1}),[56] which allows ICFES to carry more oxygen than free ICG and enables the production of more singlet oxygen upon NIR irradiation.

Photochemotoxicity of the ICFESs in vitro

Figure 3 (I) shows the living and dead B16F10 cells 24 h after different treatments. MTT analyses (Figure 3 (II)) showed 92% cell viability after exposure to NIR without ICG (Figure 3 (II), X2), suggesting that the toxicity of 5 min of NIR (808 nm; 6 W cm^{-2}) alone is negligible. On the other hand, all the drug-treated groups exhibited dose-dependent

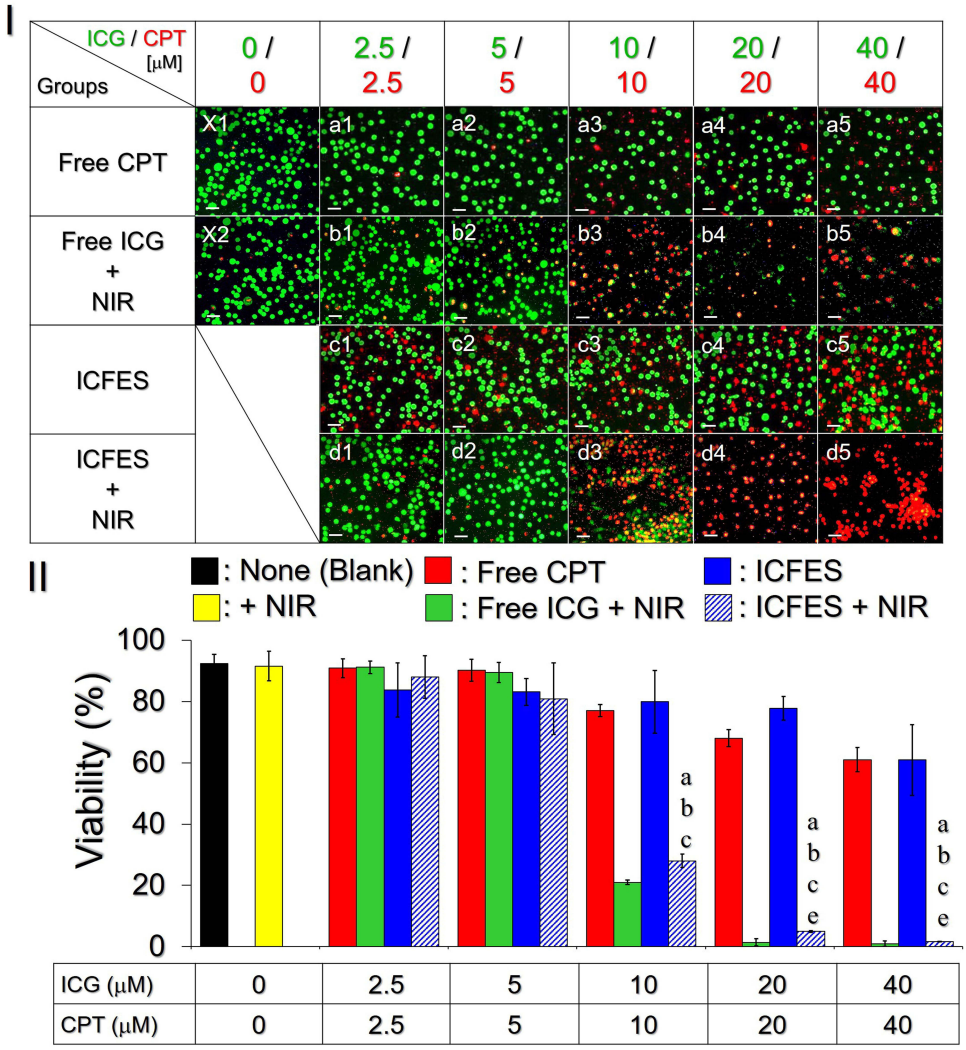

Figure 3 Photochemotherapeutic effects of the ICFESs in vitro. (A) Fluoromicrographic images of the B16F10 cells 24 h after treatment with none (X1; blank control), NIR alone (X2), free CPT (a1–a5), free ICG + NIR (b1–b5), ICFES (c1–c5), or ICFES + NIR (d1–d5). The doses of ICG and/or CPT provided by the free agents or ICFES were [ICG]/[CPT] = 0/0, 2.5/2.5, 5/5, 10/10, 20/20, and 40/40 μM, as indicated in the figure. Green and red spots indicate live and dead cells stained with calcein-AM and propidium iodide, respectively. Scale bar = 100 μm. (B) Quantitative analyses of the viability of B16F10 cells 24 h after various treatments. The values presented are the means ± SDs (n = 3). a, b, c, d, and e represent $P < 0.05$ compared to the group treated with none, NIR alone, free CPT, free ICG + NIR, and ICFES, respectively, under equal ICG and/or CPT dose setting.

https://doi.org/10.2147/IJN.S505458

decreases in cell viability (Figure 3 (I), Rows a–d), and the ICFESs without NIR displayed in vitro anticancer efficacy similar to that of free CPT at the same dose. ICFES + NIR treatment led to significantly decreased cellular viability (< 10%) at ICG/CPT doses of ≥ 20/20 μM, which was similar to the efficacy achieved with free ICG + NIR. These results clearly indicate that the ICFESs in combination with NIR irradiation destroyed cancer cells, and phototherapy played a vital role in the ICFES-mediated anticancer approach. However, using free ICG may not be appropriate in clinical practice because it has off-target effects and is susceptible to the physiological environment,[44,45] making it unfavorable for use in vivo.

Homologous Targeting and Intratumoral Retention of the ICFESs in vivo

Given that the ICFESs were rapidly taken up by cancer cells in vitro (Figure 1 (IX)), the homologous tumor targeting and intratumoral retention of the ICFESs in vivo were further assessed using the fluorescence intensity of ICG as an indicator. As presented in Figure 4 (I), the fluorescence was barely detected in the group with free ICG after intravenous injection for an hour, but marked fluorescence can be obtained in the tumors 16 h after treatment with the ICFESs according to the degree of fluorescent expression. This result was attributed to the capabilities of immune escape, cancer-targeting, and rapid cellular uptake of ICFES due to the exosomal membrane.[25–28]

Figure 4 (II) shows the results of the intratumoral assay over 7 days. ICFES fluorescence was detectable throughout the experiment, whereas that of free ICG was barely detected after 24 h, indicating that the retention of the ICFESs in tumors was significantly greater than that of the free agents. On the basis of the fluorescence intensities in the organs and tumors in situ on the 7th day after intratumoral injection (Figure 4 (III)), the ICFESs were detected in the tumors (Figure 4 (III/B, a)) and livers (Figure 4 (III/B, f)), whereas no fluorescence from free ICG was detected (Figure 4 (III/A, a–f)), which is consistent with the results shown in Figure 4 (II).

Tumoricidal Effects of the ICFESs in vivo

On the basis of the photochemotoxicity of ICFES to melanoma shown in Figure 3, ICFES with 40/40 μM ICG/CPT was used for the animal study. Figure 5 (I) shows the conditions of the mice subjected to various treatments over the 14-day experiment. Only ICFES + NIR treatment successfully suppressed tumor growth (Figure 5 (I), Row e), whereas the tumors in all the other groups (Figure 5 (I), Rows a–d) markedly grew during the 14 days. The body weights of the mice in each group did not significantly change throughout experiment (Figure 5 (II), P = NS for each). According to the measurement of tumor size plotted in Figure 5 (III), CPT and ICFES without NIR cannot inhibit the growth of melanoma,

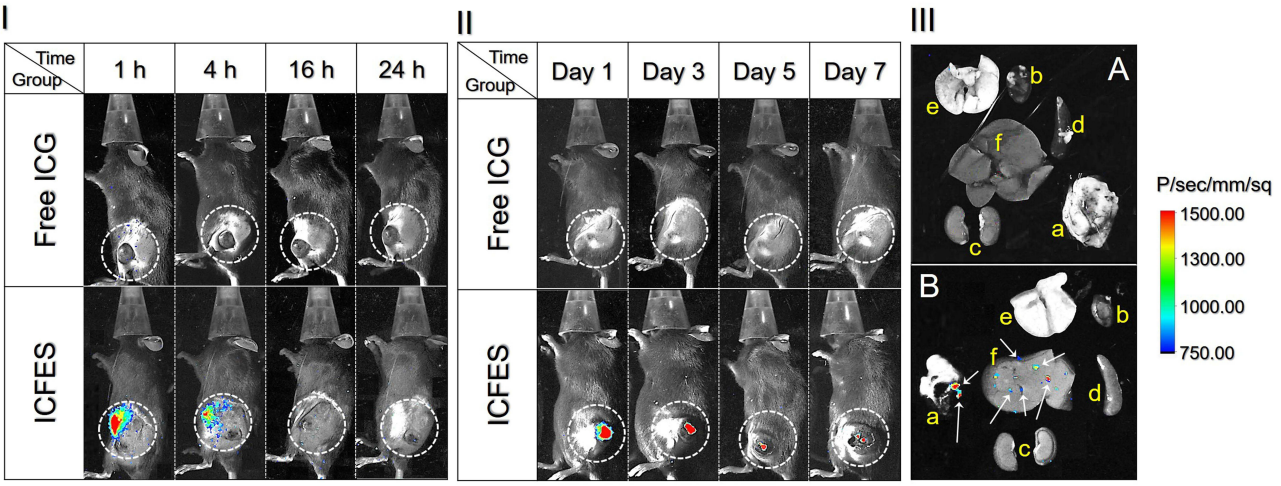

Figure 4 Tumor-targeting and retention of the ICFESs in vivo. (**I**) Time-lapse fluorescence images of ICG in B16F10 tumor-bearing mice after intravenous tail injection of free ICG or ICFESs within 24 h. (**II**) Time-lapse fluorescence images of ICG in B16F10 tumor-bearing mice after intratumoral injection of free ICG or the ICFESs within 7 days. The dashed circles in (**I**) and (**II**) indicate the positions of the tumors in vivo. (**III**) Images of ICG fluorescence in the tumors and five organs collected from the mice 7 days after intratumoral injection of free ICG (**A**) or the ICFESs (**B**). a, b, c, d, e, and f represent the tumor, heart, kidney, spleen, lung, and liver, respectively. The arrows in B indicate the locations of the ICG signals in the tumor and liver.

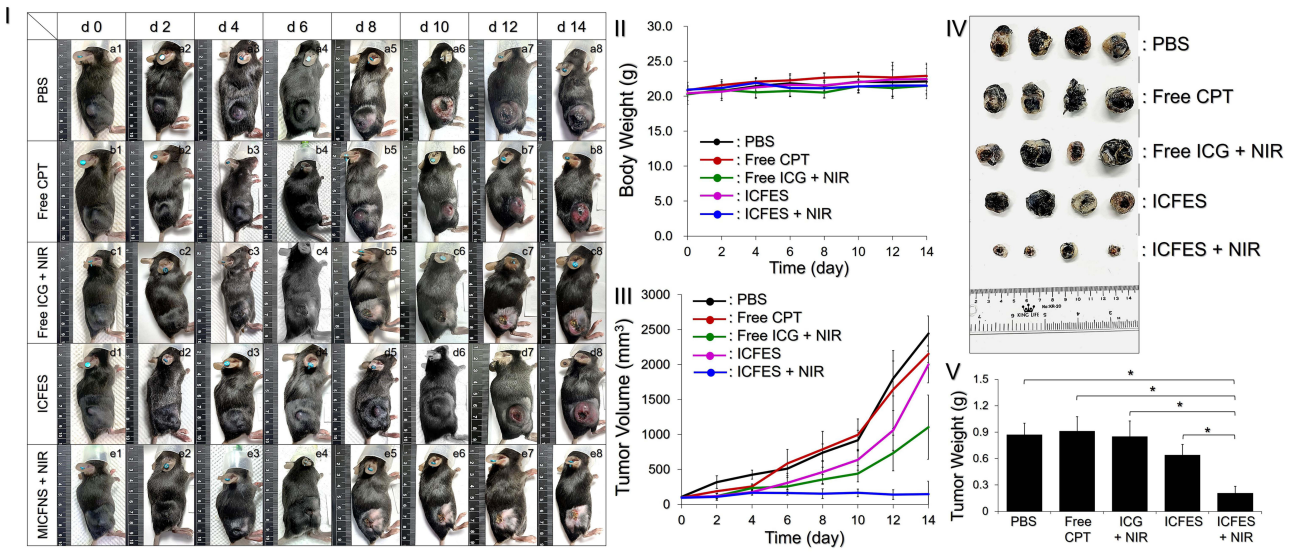

Figure 5 Anticancer effects of the ICFESs in vivo. (**I**) Appearance of the B16F10 tumor-bearing mice after 14 days of various treatments. (**II** and **III**) Variations in body weight (**II**) and tumor size (**III**) of the experimental mice within 14 days. (**IV**) Photograph of all tumors collected after sacrifice on the 14th day. (**V**) The weights of the tumors in each group after 14 days of treatment. The values in (**II**), (**III**), and (**V**) are the means ± SDs (n = 4). *P < 0.05.

resulting in 21.7 and 20.4-fold increased size of tumors, respectively, after 14 days. Free ICG + NIR was able to damage tumors, but cancer cells without irradiation remained intact and continuously grew over time, resulting in tumors with a 10.7-fold increased size after 14 days. Only ICFES + NIR treatment effectively halted melanoma cell proliferation, and the tumor size was merely enhanced by 1.5-fold after two weeks. Moreover, the above anticancer efficacies achieved by different settings can be truly verified by the real dimensions (Figure 5 (IV)) and weights (Figure 5 (V)) of tumors measured after extraction. Taken together, these findings clearly indicate that ICFESs with 40/40 μM ICG/CPT in combination with 30 sec of NIR exposure (808 nm; 6 W cm^{-2}) enabled photochemotherapy of cancer in vivo.

The anticancer efficacy of the ICFESs without NIR was greater than that of free CPT at the same concentration on the basis of tumor size (Figure 5 (III)). Such a result could be explained that because ICFES have longer intratumoral retention time than free agents (Figure 4 (II)) and thus provide higher tumoricidal efficacy. Furthermore, the ICFESs containing PFOB may oxygenate the TME and alleviate hypoxia-induced drug resistance accordingly. In addition, 40 μM CPT alone may not be sufficient for anticancer applications in vivo since less than 50% cell mortality was achieved by such a dose in vitro as illustrated in Figure 3 (B). However, CPT is critical for ICFES-mediated photochemotherapy because it can offer sustained anticancer effects by interfering the proliferation of surviving cells after phototherapy. This long-term growth inhibition is crucial for anticancer process but was not performed in the group with free ICG + NIR, resulting in grown tumors as shown in Figure 5 (III). Given that the ICFESs are equipped with both phototherapeutic and chemotherapeutic functionalities, they are certainly able to arrest the cancer progression upon NIR irradiation. Furthermore, since the ICFESs with 40 μM CPT (< IC_{50}) is sufficient for cancer treatment, they are foreseeably able to alleviate chemotoxicity and drug resistance to patients when providing tumoricidal efficacy.

Prognosis of Cancer Development After ICFES-Mediated Photochemotherapy

Figure 6 (I) shows the H&E-stained images of tumors from mice subjected to 14 days of various treatments. Except for the group with ICFES + NIR (Figure 6 (I), column e), the other four groups showed significant cancer cell proliferation and agglomeration (Figure 6 (I), columns a–d), implying that the tumors in the latter groups were growing with high integrity, and that can be reflected by their larger sizes and weights as shown in Figure 5.

Cancer progression after treatment was assessed in each group by IHC staining for caspase-3 and Ki-67 on the tumor tissues. Caspase-3 is highly involved in apoptosis and plays vital roles in both receptor- and mitochondria-mediated cell death pathways.[57] Moreover, activation of caspase-3 is necessary to trigger cancer cell apoptosis in response to various

https://doi.org/10.2147/IJN.S505458

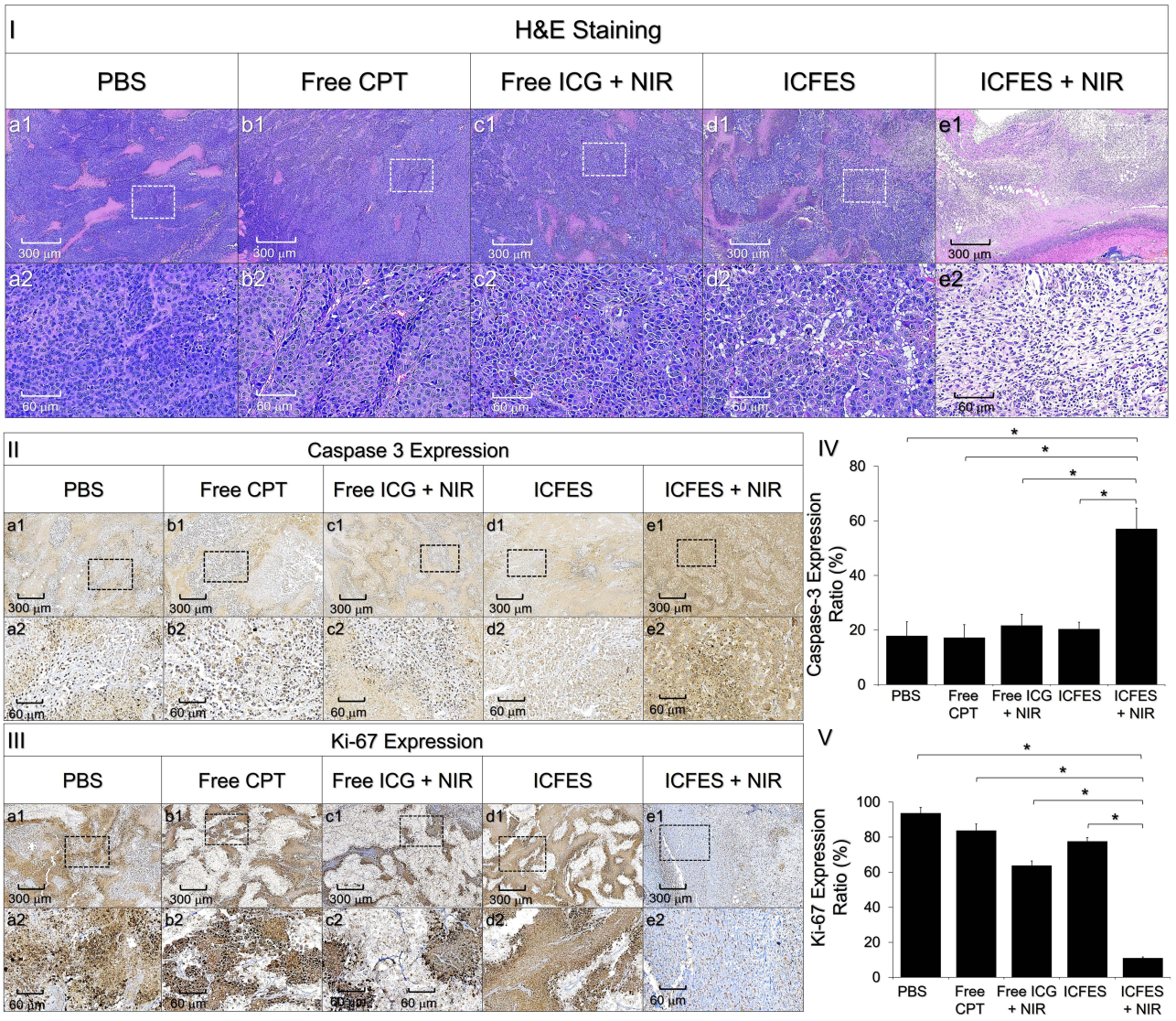

Figure 6 Histological analyses of the tumors collected after animal sacrifice. (**I–III**) Representative H&E staining images (**I**) and caspase-3 (**II**) and Ki-67 (**III**) IHC staining images of tumor tissues from each group. a2–e2 are magnified images of the areas marked in a1–e1. (**IV** and **V**) Expression levels of caspase-3 (**IV**) and Ki-67 (**V**), which are presented as percentages of the areas with marker expression, in the tumor tissues of each group. The values are presented as the means ± SDs (n = 4) *$P < 0.05$.

chemotherapeutic agents such as CPT.[58] Ki-67 is a nuclear protein that is highly expressed in growing cells but down-regulated when the cells are in the resting/G0 phase,[59] making Ki-67 a valuable biomarker for assessing cellular proliferation and cancer development.[60,61] Figure 6 (II) and (III) display the protein expression levels of caspase-3 and Ki-67 in the IHC images of the tumors from the different treatment groups. Compared with those in the other four groups, the tumors in the ICFES + NIR group presented approximately 3-fold greater expression of caspase-3 (Figure 6 (IV), $P < 0.05$ for each) and 5-fold lower expression of Ki-67 (Figure 6 (V), $P < 0.05$ for each) after 14 days of treatment, indicating that most of the cancer cells in this group had committed to apoptosis instead of proliferation after treatment. These data are consistent with the results of tumor development shown in Figure 5, suggesting that the incidence of tumor recurrence in the ICFES + NIR group is rather low. However, further validation is needed and efforts are currently in progress.

Systematic Toxicity of the ICFESs

Figure 7 (I) displays the quantitative analyses for blood cell numbers and hepatic as well as renal functions of the tumor-bearing mice before and after treatment. All of the drug-treated mice exhibited changes in marker expression levels that

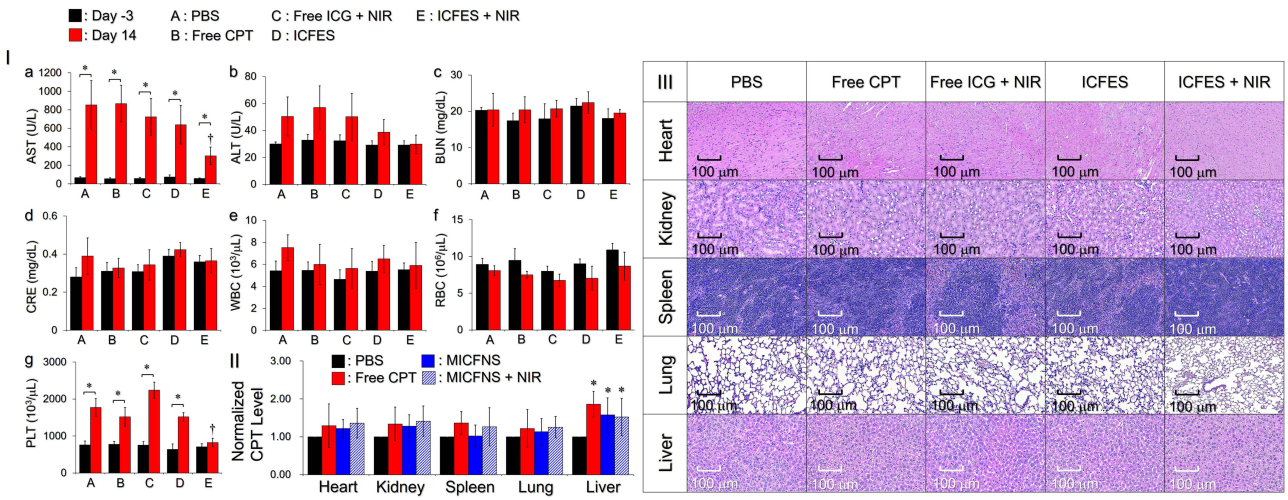

Figure 7 Systemic toxicity of the ICFESs. (**I**) Concentrations of the serum markers AST (a), ALT (b), BUN (c), and CRE (d), as well as the WBC (e), RBC (f), and PLT (f) counts of all the experimental mice measured 3 days prior to treatment (day −3) and immediately before sacrifice (day 14). The values are the means ± SDs (n = 4) $^{*}P < 0.05$; $^{\dagger}P < 0.05$ compared with the PBS group at the same time point. (B) Quantitative analysis of the amount of CPT in the hearts, kidneys, spleens, lungs, and livers of the mice after 14 days of treatment. The values are the means ± SDs (n = 4) $^{*}P < 0.05$ compared with the value obtained from the same organ in the PBS group. (**III**) Photomicrographs of H&E-stained heart, kidney, spleen, lung, and liver tissues excised from the B16F10 tumor-bearing mice with various treatments after sacrifice on the 14th day.

were similar to those in the PBS, suggesting that the modalities and dosages of the treatments were not toxic to their liver (Figure 7 (I), a and b), kidney (Figure 7 (I), c and d), or blood (Figure 7 (I), e–g) over 14 days of treatment.

However, the AST levels (Figure 7 (I/a)) and PLT counts (Figure 7 (I/g)) in the PBS, free CPT, ICG + NIR, and ICFES groups significantly increased after 14 days ($P < 0.05$ for all). In contrast, those values showed the least change in the group with ICFES + NIR and were significantly lower on the 14th day than those in the PBS group ($P < 0.05$ for both). We hypothesize that the increased expression of these two markers was likely the result of cancer progression rather than the therapeutic regimen. AST, also known as glutamate oxaloacetate transaminase (GOT), is a widely used serum marker of hepatic function, and elevated levels of AST often imply hepatic injury.[62] On the other hand, an elevated PLT count is strongly correlated with cancer progression because an increase in PLT number can promote tumoral angiogenesis and consequently enhance cancer metastasis.[63] Since melanoma is characterized by high serum PLT levels[64,65] and is one of the most typical carcinomas that may lead to liver metastasis,[66,67] the increases in AST and PLT align with the known risks and clinical syndromes.

The amounts of CPT remaining in the tumors and five other organs of the mice administered CPT (the free CPT and ICFES ± NIR groups) were analyzed to assess the systemic effects of the ICFESs (Figure 7 (II)). Compared with the amount of CPT in each organ of the PBS group, CPT may have accumulated in the liver ($P < 0.05$) but not the heart, spleen, lung, or kidney (P = NS for each) after 14 days of treatment. These data are consistent with the results described previously[68] as well as those shown in Figure 4 (III). In addition, all three drug-treated groups presented similar CPT levels in the liver (P = NS for each), implying that the developed PFC exosomal carriers did not affect CPT metabolism in vivo. Furthermore, neither noticeable lesions nor inflammatory responses were found in the five examined organs from all the drug-treated mice in comparison with those in the PBS group (Figure 7 (III)), indicating that ICFES + NIR is highly biocompatible in vivo.

Conclusions

In this study, an engineered PFC exosome carrying photosensitizers (ICG) and chemotherapeutic agents (CPT), named ICFES, was designed and fabricated for targeted cancer photochemotherapy. With the inclusion of PFOB, ICFES maintains the functional properties of exosomes and enables the increased production of singlet oxygen for PDT without limitations of the hypoxic nature of TME. Furthermore, the ICFESs encapsulating multifunctional agents decreased the effective dose of CPT and consequently reduced the chemotherapeutic drug-induced side effects. In a murine model of

https://doi.org/10.2147/IJN.S505458

melanoma, we further demonstrated that the ICFESs had homologous cancer targeting effects, a longer duration of intratumoral retention, and effective tumoricidal activity upon NIR irradiation without systemic toxicity. These inhibitory effects were thought to be achieved via a dual-stage anticancer mechanism of phototherapy followed by chemotherapy. While homologous tumor targeting and cancer photochemotherapy can also be carried out using cancer-membrane-camouflaged nanoemulsions made by multiple polymers,[69] this paper is the first report showing how exosomes can incorporate with PFC to overcome the issues of off-target drug transport, severe chemotoxicity, and TME hypoxia, and thus provide new insights into anticancer exosomics.

Data Sharing Statement

The data are available from the corresponding author upon reasonable request.

Ethical Approval Statement

All of the animal protocols complied with the guidelines reviewed and approved by the Institutional Animal Care and Use Committee at Cathay General Hospital (Taiwan ROC, approval number: CGH-IACUC-113–003). All mice were purchased from BioLASCO Taiwan Co., Ltd. (Taipei, Taiwan ROC) and housed in a specific pathogen-free environment (ventilated room, 24 ± 2 °C, 60–65% humidity).

Acknowledgments

This work was financially supported by the National Science and Technology Council, Taiwan ROC. (NSTC 113-2221-E-008-015-MY3; Y.-H. Lee) and a joint grant from National Central University and Cathay General Hospital (113-CGH-NCU-A1). The authors thank Yen-Sheng Wu from Tzong Jao Hang's Electron Microscope Laboratory, School of Medicine at Fu Jen Catholic University (New Taipei City, Taiwan ROC) for technical assistance of TEM, and Cathay General Hospital (Taipei City, Taiwan ROC) for assistance of animal operations and data analyses.

Disclosure

The authors declare no competing interests.

References

1. Lee YH, Ma YT. Synthesis, characterization, and biological verification of anti-HER2 indocyanine green-doxorubicin-loaded polyethyleneimine-coated perfluorocarbon double nanoemulsions for targeted photochemotherapy of breast cancer cells. *J Nanobiotechnology*. 2017;15(1):41. doi:10.1186/s12951-017-0274-5
2. Amaral SI, Silva FALS, Costa-Almeida R, et al. Pharmaceutical formulations containing graphene and 5-fluorouracil for light-emitting diode-based photochemotherapy of skin cancer. *ACS Appl Mater Interfaces*. 2024;16(4):4333–4347. doi:10.1021/acsami.3c13409
3. Zhang Y, Xia Q, Wu T, et al. A novel multi-functionalized multicellular nanodelivery system for non-small cell lung cancer photochemotherapy. *J Nanobiotechnology*. 2021;19(1):245. doi:10.1186/s12951-021-00977-3
4. Lee JS, Kim J, Ye YS, Kim TI. Materials and device design for advanced phototherapy systems. *Adv Drug Deliv Rev*. 2022;186:114339. doi:10.1016/j.addr.2022.114339
5. Jaque D, Martinez Maestro L, Del Rosal B, et al. Nanoparticles for photothermal therapies. *Nanoscale*. 2014;6(16):9494–9530. doi:10.1039/C4NR00708E
6. Zhang Y, Zhan X, Xiong J, et al. Temperature-dependent cell death patterns induced by functionalized gold nanoparticle photothermal therapy in melanoma cells. *Sci Rep*. 2018;8(1):8720. doi:10.1038/s41598-018-26978-1
7. Castano AP, Demidova TN, Hamblin MR. Mechanisms in photodynamic therapy: part three—photosensitizer pharmacokinetics, biodistribution, tumor localization and modes of tumor destruction. *Photodiagnosis Photodyn Ther*. 2005;2(2):91–106. doi:10.1016/S1572-1000(05)00060-8
8. Benov L. Photodynamic therapy: current status and future directions. *Med Princ Pract*. 2015;24(Suppl 1):14–28. doi:10.1159/000362416
9. Lee YH, Kuo PW, Chen CJ, Sue CJ, Hsu YF, Pan MC. Indocyanine green-camptothecin Co-loaded perfluorocarbon double-layer nanocomposite: a versatile nanotheranostics for photochemotherapy and FDOT diagnosis of breast cancer. *Pharmaceutics*. 2021;13(9):1499. doi:10.3390/pharmaceutics13091499
10. Zou J, Li L, Yang Z, Chen X. Phototherapy meets immunotherapy: a win–win strategy to fight against cancer. *Nanophotonics*. 2021;10(12):3229–3245. doi:10.1515/nanoph-2021-0209
11. Sadozai H, Acharjee A, Kayani HZ, Gruber T, Gorczynski RM, Burke B. High hypoxia status in pancreatic cancer is associated with multiple hallmarks of an immunosuppressive tumor microenvironment. *Front Immunol*. 2024;15:1360629. doi:10.3389/fimmu.2024.1360629
12. Mittal V, El Rayes T, Narula N, McGraw TE, Altorki NK, Barcellos-Hoff MH. The microenvironment of lung cancer and therapeutic implications. *Adv Exp Med Biol*. 2016;890:75–110.
13. Semenza GL. The hypoxic tumor microenvironment: a driving force for breast cancer progression. *Biochim Biophys Acta*. 2016;1863(3):382–391. doi:10.1016/j.bbamcr.2015.05.036

14. Michaylira CZ, Nakagawa H. Hypoxic microenvironment as a cradle for melanoma development and progression. *Cancer Biol Ther*. 2006;5 (5):476–479. doi:10.4161/cbt.5.5.2749
15. Chen Z, Han F, Du Y, Shi H, Zhou W. Hypoxic microenvironment in cancer: molecular mechanisms and therapeutic interventions. *Signal Transduct Target Ther*. 2023;8(1):70. doi:10.1038/s41392-023-01332-8
16. Infantino V, Santarsiero A, Convertini P, Todisco S, Iacobazzi V. Cancer cell metabolism in hypoxia: role of HIF-1 as key regulator and therapeutic target. *Int J Mol Sci*. 2021;22(11):5703. doi:10.3390/ijms22115703
17. Belisario DC, Kopecka J, Pasino M, et al. Hypoxia dictates metabolic rewiring of tumors: implications for chemoresistance. *Cells*. 2020;9 (12):2598. doi:10.3390/cells9122598
18. Minassian LM, Cotechini T, Huitema E, Graham CH. Hypoxia-induced resistance to chemotherapy in cancer. *Adv Exp Med Biol*. 2019;1136:123–139.
19. Thews O, Riemann A. Tumor pH and metastasis: a malignant process beyond hypoxia. *Cancer Metastasis Rev*. 2019;38(1–2):113–129. doi:10.1007/s10555-018-09777-y
20. Wan Y, Fu LH, Li C, Lin J, Huang P. Conquering the hypoxia limitation for photodynamic therapy. *Adv Mater*. 2021;33(48):e2103978. doi:10.1002/adma.202103978
21. Jain KK. Nanomedicine: application of nanobiotechnology in medical practice. *Med Princ Pract*. 2008;17:89–101. doi:10.1159/000112961
22. Yang B, Chen Y, Shi J. Exosome biochemistry and advanced nanotechnology for next-generation theranostic platforms. *Adv Mater*. 2019;31(2): e1802896. doi:10.1002/adma.201802896
23. Zhang Y, Bi J, Huang J, Tang Y, Du S, Li P. Exosome: a review of its classification, isolation techniques, storage, diagnostic and targeted therapy applications. *Int J Nanomed*. 2020;15:6917–6934. doi:10.2147/IJN.S264498
24. Isola AL, Chen S. Exosomes: the messengers of health and disease. *Curr Neuropharmacol*. 2017;15(1):157–165. doi:10.2174/1570159X14666160825160421
25. Tian T, Zhu YL, Hu FH, Wang YY, Huang NP, Xiao ZD. Dynamics of exosome internalization and trafficking. *J Cell Physiol*. 2013;228 (7):1487–1495. doi:10.1002/jcp.24304
26. Samanta S, Rajasingh S, Drosos N, Zhou Z, Dawn B, Rajasingh J. Exosomes: new molecular targets of diseases. *Acta Pharmacol Sin*. 2018;39 (4):501–513. doi:10.1038/aps.2017.162
27. Edelmann MJ, Kima PE. Current understanding of extracellular vesicle homing/tropism. *Zoonoses*. 2022;2:14. doi:10.15212/ZOONOSES-2022-0004
28. Qiao L, Hu S, Huang K, et al. Tumor cell-derived exosomes home to their cells of origin and can be used as Trojan horses to deliver cancer drugs. *Theranostics*. 2020;10(8):3474–3487. doi:10.7150/thno.39434
29. Jeong K, Yu YJ, You JY, Rhee WJ, Kim JA. Exosome-mediated microRNA-497 delivery for anti-cancer therapy in a microfluidic 3D lung cancer model. *Lab Chip*. 2020;20(3):548–557. doi:10.1039/C9LC00958B
30. Yu S, Liao R, Bai L, et al. Anticancer effect of hUC-MSC-derived exosome-mediated delivery of PMO-miR-146b-5p in colorectal cancer. *Drug Deliv Transl Res*. 2024;14(5):1352–1369. doi:10.1007/s13346-023-01469-7
31. Fujimura NA, Fatima SE, Ahmed N, et al. Evaluation of exosomes encapsulated recombinant Interleukin-29 for its in vitro anticancer studies. *J Biotechnol*. 2023;373:24–33. doi:10.1016/j.jbiotec.2023.06.008
32. Yim N, Ryu SW, Choi K, et al. Exosome engineering for efficient intracellular delivery of soluble proteins using optically reversible protein-protein interaction module. *Nat Commun*. 2016;7:12277. doi:10.1038/ncomms12277
33. Pullan J, Dailey K, Bhallamudi S, et al. Modified bovine milk exosomes for doxorubicin delivery to triple-negative breast cancer cells. *ACS Appl Bio Mater*. 2022;5(5):2163–2175. doi:10.1021/acsabm.2c00015
34. Chen J, Cao F, Cao Y, Wei S, Zhu X, Xing W. Targeted therapy of lung adenocarcinoma by the nanoplatform based on milk exosomes loaded with paclitaxel. *J Biomed Nanotechnol*. 2022;18(4):1075–1083. doi:10.1166/jbn.2022.3278
35. Vankayala R, Hwang KC. Near-infrared-light-activatable nanomaterial-mediated phototheranostic nanomedicines: an emerging paradigm for cancer treatment. *Adv Mater*. 2018;30(23):e1706320. doi:10.1002/adma.201706320
36. Rudolf E, Rudolf K, Cervinka M. Camptothecin induces p53-dependent and -independent apoptogenic signaling in melanoma cells. *Apoptosis*. 2011;16(11):1165–1176. doi:10.1007/s10495-011-0635-8
37. Lian C, Cao S, Zeng W, et al. RJT-101, a novel camptothecin derivative, is highly effective in the treatment of melanoma through DNA damage by targeting topoisomerase 1. *Biochem Pharmacol*. 2020;171:113716. doi:10.1016/j.bcp.2019.113716
38. Jung JJ, Yu DJG, Ito K, Rofagha S, Lee SS, Hoang QV. Quantitative assessment of asymmetric choroidal outflow in pachychoroid eyes on ultra-widefield indocyanine green angiography. *Invest Ophthalmol Vis Sci*. 2020;61(8):50. doi:10.1167/iovs.61.8.50
39. Son GM, Ahn HM, Lee IY, Ha GW. Multifunctional indocyanine green applications for fluorescence-guided laparoscopic colorectal surgery. *Ann Coloproctol*. 2021;37(3):133–140. doi:10.3393/ac.2021.05.07
40. Ganau M, Iqbal M, Ligarotti GKI, Syrmos N. Breakthrough in the assessment of cerebral perfusion and vascular permeability after brain trauma through the adoption of dynamic indocyanine green-enhanced near-infrared spectroscopy. *Quant Imaging Med Surg*. 2020;10(11):2081–2084. doi:10.21037/qims-20-905
41. Lee YH, Pham UNT. Engineered indocyanine green and PD-L1 inhibitors Co-Loaded perfluorochemical double-layered nanodroplets offer effective photoimmunotherapy against colorectal cancer. *Chem Eng J*. 2023;460:141819. doi:10.1016/j.cej.2023.141819
42. Xu HL, ZhuGe DL, Chen PP, et al. Silk fibroin nanoparticles dyeing indocyanine green for imaging-guided photo-thermal therapy of glioblastoma. *Drug Deliv*. 2018;25(1):364–375. doi:10.1080/10717544.2018.1428244
43. Hong F, Park JS, Kim SW, Park SJ, Kim SK. Near-infrared phototherapy for patient-derived orthotopic xenograft model of hepatocellular carcinoma in combination with indocyanine green. *J Photochem Photobiol B*. 2020;209:111938. doi:10.1016/j.jphotobiol.2020.111938
44. Wang H, Li X, Tse BW, et al. Indocyanine green-incorporating nanoparticles for cancer theranostics. *Theranostics*. 2018;8(5):1227–1242. doi:10.7150/thno.22872
45. Saxena V, Sadoqi M, Shao J. Degradation kinetics of indocyanine green in aqueous solution. *J Pharm Sci*. 2003;92(10):2090–2097. doi:10.1002/jps.10470
46. Lowe KC. Perfluorochemical respiratory gas carriers: benefits to cell culture systems. *J Fluor Chem*. 2002;118:19–26. doi:10.1016/S0022-1139(02)00200-2

47. Shu S, Allen CL, Benjamin-Davalos S, et al. A rapid exosome isolation using ultrafiltration and size exclusion chromatography (REIUS) method for exosome isolation from melanoma cell lines. *Methods Mol Biol*. 2021;2265:289–304.
48. Fraker CA, Mendez AJ, Inverardi L, Ricordi C, Stabler CL. Optimization of perfluoro nano-scale emulsions: the importance of particle size for enhanced oxygen transfer in biomedical applications. *Colloids Surf B Biointerfaces*. 2012;98:26–35. doi:10.1016/j.colsurfb.2012.04.011
49. Slaoui M, Fiette L. Histopathology procedures: from tissue sampling to histopathological evaluation. *Methods Mol Biol*. 2011;691:69–82.
50. Rezaie J, Feghhi M, Etemadi T. A review on exosomes application in clinical trials: perspective, questions, and challenges. *Cell Commun Signal*. 2022;20(1):145. doi:10.1186/s12964-022-00959-4
51. Qian X, Xie F, Cui D. Exploring purification methods of exosomes from different biological samples. *Biomed Res Int*. 2023;2023:2336536. doi:10.1155/2023/2336536
52. Xi XM, Xia SJ, Lu R. Drug loading techniques for exosome-based drug delivery systems. *Pharmazie*. 2021;76(2):61–67. doi:10.1691/ph.2021.0128
53. Baghban N, Kodam SP, Ullah M. Role of CD9 sensing, AI, and exosomes in cellular communication of cancer. *Int J Stem Cell Res Ther*. 2023;10 (1):079. doi:10.23937/2469-570X/1410079
54. Suga K, Matsui D, Watanabe N, Okamoto Y, Umakoshi H. Insight into the exosomal membrane: from viewpoints of membrane fluidity and polarity. *Langmuir*. 2021;37(38):11195–11202. doi:10.1021/acs.langmuir.1c00687
55. Ferreira BM, Ramalho JB, Lucas EF. Demulsification of water-in-crude oil emulsions by microwave radiation: effect of aging, demulsifier addition, and selective heating. *Energy Fuels*. 2013;27(2):615–621. doi:10.1021/ef301110m
56. Chin K, Khattak SF, Bhatia SR, Roberts SC. Hydrogel-perfluorocarbon composite scaffold promotes oxygen transport to immobilized cells. *Biotechnol Prog*. 2008;24(2):358–366. doi:10.1021/bp070160f
57. Asadi M, Taghizadeh S, Kaviani E, et al. Caspase-3: structure, function, and biotechnological aspects. *Biotechnol Appl Biochem*. 2022;69 (4):1633–1645. doi:10.1002/bab.2233
58. Rodríguez-Hernández A, Brea-Calvo G, Fernández-Ayala DJ, Cordero M, Navas P, Sánchez-Alcázar JA. Nuclear caspase-3 and caspase-7 activation, and poly(ADP-ribose) polymerase cleavage are early events in camptothecin-induced apoptosis. *Apoptosis*. 2006;11(1):131–139. doi:10.1007/s10495-005-3276-y
59. Gerdes J, Lemke H, Baisch H, Wacker HH, Schwab U, Stein H. Cell cycle analysis of a cell proliferation-associated human nuclear antigen defined by the monoclonal antibody Ki-67. *J Immunol*. 1984;133(4):1710–1715. doi:10.4049/jimmunol.133.4.1710
60. Liu Q, Peng Z, Shen L, Shen L. Prognostic and clinicopathological value of Ki-67 in melanoma: a meta-analysis. *Front Oncol*. 2021;11:737760. doi:10.3389/fonc.2021.737760
61. Moltajaei MH, Pourzare Mehrbani S, Motahari P, Rezapour R. Clinicopathological and prognostic value of Ki-67 expression in oral malignant melanoma: a systematic review and meta-analysis. *J Dent Res Dent Clin Dent Prospects*. 2022;16(3):140–146. doi:10.34172/joddd.2022.024
62. Vella SJ, Beattie P, Cademartiri R, et al. Measuring markers of liver function using a micropatterned paper device designed for blood from a fingerstick. *Anal Chem*. 2012;84(6):2883–2891. doi:10.1021/ac203434x
63. Wojtukiewicz MS, Sierko E, Hempel E, Tucker SC, Honn KV. Platelets and cancer angiogenesis nexus. *Cancer Metastasis Rev*. 2017;36 (2):249–262. doi:10.1007/s10555-017-9673-1
64. Tas F, Ciftci R, Kilic L, et al. Clinical and prognostic significance of coagulation assays in melanoma. *Melanoma Res*. 2012;22(5):368–375. doi:10.1097/CMR.0b013e328357be7c
65. Rachidi S, Kaur M, Lautenschlaeger T, Li Z. Platelet count correlates with stage and predicts survival in melanoma. *Platelets*. 2019;30 (8):1042–1046. doi:10.1080/09537104.2019.1572879
66. Tsilimigras DI, Brodt P, Clavien PA, et al. Liver metastases. *Nat Rev Dis Primers*. 2021;7(1):27. doi:10.1038/s41572-021-00261-6
67. Agarwala SS, Eggermont AM, O'Day S, Zager JS. Metastatic melanoma to the liver: a contemporary and comprehensive review of surgical, systemic, and regional therapeutic options. *Cancer*. 2014;120(6):781–789. doi:10.1002/cncr.28480
68. Platzer P, Thalhammer T, Hamilton G, et al. Metabolism of camptothecin, a potent topoisomerase I inhibitor, in the isolated perfused rat liver. *Cancer Chemother Pharmacol*. 2000;45(1):50–54. doi:10.1007/PL00006742
69. Lee YH, Chen CS. Carcinomembrane-camouflaged perfluorochemical dual-layer nanopolymersomes bearing indocyanine green and camptothecin effectuate targeting photochemotherapy of cancer. *ACS Biomater Sci Eng*. 2024;10(10):6332–6343. doi:10.1021/acsbiomaterials.4c01150